Subsalt imaging by target-oriented wavefield least-squares migration: A 3-D field-data example

Yaxun Tang and Biondo Biondi

ABSTRACT

We pose the reflectivity-imaging problem as a linear inversion problem and solve it in the image domain in a target-oriented fashion. The most computationally intensive part of the image-domain inversion is the explicit computation of the Hessian matrix. We show how we can overcome the cost issue by using the phase-encoding technique in the 3-D conical-wave domain. We apply the inversion-based imaging methodology to a 3-D field data set acquired from the Gulf of Mexico (GOM), and we precondition the inversion with non-stationary dip filters, which naturally incorporate interpreted geological information. Numerical examples demonstrate that imaging by regularized inversion successfully recovers the reflectivities from the effects of uneven illumination, yielding images with more balanced amplitudes and higher spatial resolution.

INTRODUCTION

Successful geological interpretation requires accurate reflectivity images of the subsurface. Reflectivity images obtained by prestack depth migration, however, are often distorted by uneven subsurface illumination. This is because the migration operator is only the adjoint of the forward Born modeling operator (Lailly, 1983), which is non-unitary due to the limited acquisition geometry, complex overburden and band-limited wavefields. The distorted image, as exemplified by biased amplitudes and the shadow zone effect, presents significant difficulties for accurate geological interpretation.

To correct the effects of uneven illumination, the reflectivity imaging problem can be posed as a linear inverse problem, which, instead of using the adjoint operator, uses the pseudo-inverse of the Born modeling operator to optimally reconstruct the reflectivity. This inversion-based imaging method is also widely known as least-squares migration (Nemeth et al., 1999; Kühl and Sacchi, 2003; Clapp, 2005; Valenciano, 2008).

Least-squares migration can be implemented in either the data domain or the image domain. In this paper, we focus on the image-domain inversion scheme because it can be implemented in a target-oriented fashion and hence is more suitable for large-scale 3-D applications. The target-oriented image-domain formulation allows us to

invert only areas of particular interest, enabling accurate imaging at the reservoir level.

As shown by Valenciano (2008), image-domain least-squares migration contains three main steps: (1) compute the migrated image for a chosen target area, (2) compute the Hessian, the normal operator of the Born modeling operator, for the same target area, and (3) deblur the migrated image using the Hessian with an iterative solver. Among the three steps, the explicit computation of the Hessian is the most computationally intensive part, because it requires either storing a huge number of Green's functions for reuse (Valenciano, 2008), or performing a large number of wavefield propagations. (Each receiver-side Green's function has to be recomputed for each shot, if the Green's functions are not stored) (Tang and Lee, 2010). Fortunately, the computational cost can be drastically reduced by using the phase-encoding method, which does not require storing any Green's functions and significantly reduces the required number of wavefield propagations (Tang, 2009). In this paper, we extend phase-encoding theory to 3-D and show how the cost of Hessian can be drastically reduced by using a simultaneous phase-encoding scheme in the 3-D conical-wave domain.

Regularization is a crucial component of solving an ill-posed inverse problem. One important advantage of the image-domain inversion scheme is that solving the linear inversion problem (step 3) is very fast, which involves only sparse-matrix and vector multiplications. Therefore, different regularization parameters or schemes can be tried at very low cost. The high efficiency of this method also makes interpretation-driven interactive reflectivity imaging possible, where we can repeat the inversion with regularizations that incorporate different geological scenarios and obtain the results in almost real time. In this paper, we precondition the inversion problem with non-stationary dip filters (Clapp, 2003; Hale, 2007; Claerbout, 2008), which impose smoothness on the reflectivities along given dip directions. We show that the dip filter naturally incorporates prior knowledge based on interpreter's geological interpretation into the inversion, and it helps the inversion converge to a geologically meaningful result.

This paper is organized as follows: we first review the theory of image-domain least-squares migration. Then we show how the phase-encoded Hessian can be efficiently computed in the 3-D conical-wave domain. Following that, we discuss how to precondition the inversion with dip filters. Finally, we apply the method to a 3-D field data set acquired from the Gulf of Mexico (GOM), where we invert subsalt reflectivities in a target-oriented fashion.

THEORY

Image-domain least-squares migration

Image-domain least-squares migration (Valenciano, 2008; Tang, 2009) optimizes the reflectivity model by minimizing an objective function defined in the image domain as follows:

$$J(\mathbf{m}) = \frac{1}{2}||\mathbf{Hm} - \mathbf{m}_{\text{mig}}||^2 + \epsilon\mathcal{R}(\mathbf{m}), \tag{1}$$

where $\mathbf{m}$ is the reflectivity model, and $\mathbf{m}_{\text{mig}}$ is the migrated image

$$\mathbf{m}_{\text{mig}} = \mathbf{L}^*\mathbf{d}_{\text{obs}}, \tag{2}$$

where * denotes taking the adjoint, $\mathbf{d}_{\text{obs}}$ is the vector of observed primaries, and $\mathbf{L}$ is the Born modeling operator, which models only singly scattered waves. In equation 1, $\mathbf{H} = \mathbf{L}^*\mathbf{L}$ is the Hessian operator, which contains all necessary information, including information of acquisition geometry, velocity model and frequency content of seismic waves, for correcting the effects of distorted illumination. The second term $\mathcal{R}(\mathbf{m})$ in equation 1 is a regularization term that incorporates user-defined model covariance into the inversion, and ϵ determines the strength of the regularization. Objective function J can be minimized with any iterative solver, such as the conjugate gradient method. The most important components in minimizing J are the explicit calculation of the Hessian operator $\mathbf{H}$ and the definition of the regularization term $\mathcal{R}(\mathbf{m})$. In the subsequent subsections, we first demonstrate how to calculate the Hessian $\mathbf{H}$ efficiently in 3-D. Then we discuss how to incorporate dip constraints into the inversion and solve it as a preconditioning problem.

The 3-D phase-encoded Hessian

3-D conical-wave migration (Whitmore, 1995; Duquet et al., 2001; Zhang et al., 2005; Liu et al., 2006) has been widely used to migrate marine streamer data sets. In this section, we demonstrate how the Hessian can be efficiently computed in this domain using simultaneous phase encoding, which encodes both source- and receiver-side Green's functions.

As derived in Appendix A, each component of the the 3-D conical-wave domain Hessian reads

$$\begin{aligned} H(\mathbf{x},\mathbf{x}') &= \sum_{\omega}|\omega|^5\sum_{y_s}\sum_{p_{s_x}}\sum_{\mathbf{x}_r} G(\mathbf{x},\mathbf{x}_r,\omega)G^*(\mathbf{x}',\mathbf{x}_r,\omega) \\ &\quad \sum_{x_s} W(\mathbf{x}_r,x_s,y_s)f_s(\omega)G(\mathbf{x},x_s,y_s,\omega)\mathrm{e}^{i\omega p_{s_x}x_s} \\ &\quad \sum_{x'_s} W(\mathbf{x}_r,x'_s,y_s)f^*_s(\omega)G^*(\mathbf{x}',x'_s,y_s,\omega)\mathrm{e}^{-i\omega p_{s_x}x'_s}, \end{aligned} \tag{3}$$

where $f_s(\omega)$ is the source signature at frequency ω; x_s and y_s are the source locations in the inline and crossline directions, respectively; $\mathbf{x}_r = (x_r, y_r, 0)$ is the receiver location; p_{s_x} is the horizontal component of the source ray parameter; $W(\mathbf{x}_r, x_s, y_s)$ is the acquisition mask operator, which contains ones where we record data, and zeros where we do not; and $G(\mathbf{x}, x_s, y_s, \omega)$ and $G(\mathbf{x}, \mathbf{x}_r, \omega)$ are the Green's functions connecting the source and receiver positions to the image point $\mathbf{x} = (x, y, z)$, respectively.

The diagonal part of the Hessian (when $\mathbf{x} = \mathbf{x}'$), which contains autocorrelations of both source and receiver-side Green's functions, can be interpreted as a subsurface illumination map with contributions from both sources and receivers. The rows of the Hessian (for fixed $\mathbf{x}$'s and varying $\mathbf{x}'$), which contains crosscorrelations of both source and receiver-side Green's functions, can be interpreted as resolution functions (Lecomte, 2008; Tang, 2009). They measure how much smearing an image can have due to a given acquisition setup.

The exact Hessian defined by equation 3, however, is nontrivial and very expensive to implement. It requires either storing a huge number of Green's functions for reuse, or performing a large number of wavefield propagations to repeatedly calculate the Green's functions, resulting in a computational cost proportional to $N_{y_s} N_{p_{s_x}} N_{x_r} N_{y_r}$, with N_{y_s}, $N_{p_{s_x}}$, N_{x_r} and N_{y_r} being the number of crossline shots, inline conical waves, inline receivers and crossline receivers, respectively.

In order to reduce the computational cost, we use the simultaneous phase-encoding technique to efficiently calculate an approximate version of equation 3. The simultaneous phase-encoding, however, is only strictly valid when the acquisition mask operator is independent along the encoding axes (Tang, 2009). For the 3-D conical-wave-domain Hessian, the encoding axes are the inline source axis x_s and the receiver axis $\mathbf{x}_r = (x_r, y_r)$, respectively. Ocean-bottom cable (OBC) and land acquisition geometries, where receivers are fixed for all sources, obviously satisfy this condition. But marine-streamer acquisition geometry, where the receiver cable moves with sources, apparently does not. To make the theory applicable to the marine-streamer data case, we assume that the receiver location $\mathbf{x}_r$ depends only on the crossline source position y_s, but is independent of the inline source position x_s. This implicitly assumes that for a fixed crossline y_s, all inline shots share the same receiver array. Therefore, we can express the acquisition mask operator as a product of two separate functions:

$$W(\mathbf{x}_r, x_s, y_s) \approx W_r(\mathbf{x}_r, y_s) W_s(x_s, y_s), \tag{4}$$

where W_r and W_s define the distributions of receiver position $\mathbf{x}_r$ and the inline source position x_s, respectively, for a given crossline source position y_s.

Substituting equation 4 into equation 3 yields

$$\begin{aligned} H(\mathbf{x}, \mathbf{x}') \;=\; & \sum_{\omega} |\omega|^5 \sum_{y_s} \sum_{p_{s_x}} \sum_{\mathbf{x}_r} W_r(\mathbf{x}_r, y_s) G(\mathbf{x}, \mathbf{x}_r, \omega) G^*(\mathbf{x}', \mathbf{x}_r, \omega) \\ & \sum_{x_s} W_s(x_s, y_s) f_s(\omega) G(\mathbf{x}, x_s, y_s, \omega) \mathrm{e}^{i\omega p_{s_x} x_s} \\ & \sum_{x'_s} W_s(x'_s, y_s) f_s^*(\omega) G^*(\mathbf{x}', x'_s, y_s, \omega) \mathrm{e}^{-i\omega p_{s_x} x'_s}. \end{aligned} \tag{5}$$

With further encoding on the receiver-side Green's functions, we obtain the simultaneously phase-encoded Hessian as follows:

$$\begin{aligned}\widetilde{\widetilde{H}}(\mathbf{x},\mathbf{x}',\mathbf{p}_r) &= \sum_{\omega}|\omega|^5\sum_{y_s}\sum_{p_{s_x}} \\ &\times\sum_{\mathbf{x}_r}W_r(\mathbf{x}_r,y_s)G(\mathbf{x},\mathbf{x}_r,\omega)\alpha(\mathbf{x}_r,\mathbf{p}_r,\omega) \\ &\times\sum_{\mathbf{x}'_r}W_r(\mathbf{x}'_r,y_s)G^*(\mathbf{x}',\mathbf{x}'_r,\omega)\alpha(\mathbf{x}'_r,\mathbf{p}_r,\omega) \\ &\times\sum_{x_s}W_s(x_s,y_s)f_s(\omega)G(\mathbf{x},x_s,y_s,\omega)\mathrm{e}^{i\omega p_{s_x}x_s} \\ &\times\sum_{x'_s}W_s(x'_s,y_s)f_s^*(\omega)G^*(\mathbf{x}',x'_s,y_s,\omega)\mathrm{e}^{-i\omega p_{s_x}x'_s},\end{aligned} \tag{6}$$

where α is the receiver-side encoding function, to be specified later. Equation 6 can be greatly simplified as follows:

$$\begin{aligned}\widetilde{\widetilde{H}}(\mathbf{x},\mathbf{x}',\mathbf{p}_r) &= \sum_{\omega}|\omega|^5\sum_{y_s}\sum_{p_{s_x}}S(\mathbf{x},p_{s_x},y_s,\omega)S^*(\mathbf{x}',p_{s_x},y_s,\omega) \\ &\quad R(\mathbf{x},p_{s_x},y_s,\mathbf{p}_r,\omega)R^*(\mathbf{x}',p_{s_x},y_s,\mathbf{p}_r,\omega),\end{aligned} \tag{7}$$

if we define

$$S(\mathbf{x},p_{s_x},y_s,\omega)=\sum_{x_s}W_s(x_s,y_s)f_s(\omega)G(\mathbf{x},x_s,y_s,\omega)\mathrm{e}^{i\omega p_{s_x}x_s}, \tag{8}$$

and

$$R(\mathbf{x},p_{s_x},y_s,\mathbf{p}_r,\omega)=\sum_{\mathbf{x}_r}W_r(\mathbf{x}_r,y_s)G(\mathbf{x},\mathbf{x}_r,\omega)\alpha(\mathbf{x}_r,\mathbf{p}_r,\omega). \tag{9}$$

For one-way wave-equation-based applications, S and R can be obtained by solving the following one-way wave equations:

$$\begin{cases}\left(\frac{\partial}{\partial z}-i\sqrt{\frac{\omega^2}{v^2(\mathbf{x})}+\nabla^2}\right)S(\mathbf{x},p_{s_x},y_s,\omega)=0 \\ S(x,y,z=0,p_{s_x},y_s,\omega)=\sum_{x_s}W_s(x_s,y_s)\delta(x-x_s,y-y_s)f_s(\omega)\mathrm{e}^{i\omega p_{s_x}x_s}\end{cases}. \tag{10}$$

and

$$\begin{cases}\left(\frac{\partial}{\partial z}-i\sqrt{\frac{\omega^2}{v^2(\mathbf{x})}+\nabla^2}\right)R(\mathbf{x},p_{s_x},y_s,\mathbf{p}_r,\omega)=0 \\ R(x,y,z=0,p_{s_x},y_s,\mathbf{p}_r,\omega)=\sum_{\mathbf{x}_r}W_r(\mathbf{x}_r,y_s)\delta(x-x_r,y-y_r)\alpha(\mathbf{x}_r,\mathbf{p}_r,\omega)\end{cases}. \tag{11}$$

In both equations 10 and 11, $v(\mathbf{x})$ is the velocity at image point $\mathbf{x}$, $\nabla^2=\frac{\partial^2}{\partial x^2}+\frac{\partial^2}{\partial y^2}$ is the Laplacian operator, and $\delta(\cdot)$ is the Dirac delta function. Therefore, S is the wavefield generated by propagating the conical-wave source $\sum_{x_s}W_s(x_s,y_s)\delta(x-x_s,y-y_s)f_s(\omega)\mathrm{e}^{i\omega p_{s_x}x_s}$, whereas R is the wavefield generated by propagating the encoded-area source $\sum_{\mathbf{x}_r}W_r(\mathbf{x}_r,y_s)\delta(x-x_r,y-y_r)\alpha(\mathbf{x}_r,\mathbf{p}_r,\omega)$. It is quite obvious that the computational cost of equation 7 is independent of the number of receivers, as opposed to equation 3, for which the cost is proportional to the number of receivers.

However, the phase-encoded Hessian brings unwanted crosstalk. This becomes clear by comparing equations 6 and 3. The crosstalk can be suppressed by carefully choosing the phase-encoding function α (Tang, 2009). In this paper, we choose α to be a random phase-encoding function; thus $\mathbf{p}_r$ denotes the realization index of the random phase-encoding function. It would be very easy to verify that, with this choice of encoding functions, the expectation of the crosstalk becomes zero. Therefore, equation 6 converges to equation 5 by stacking over $\mathbf{p}_r$, according to the law of large numbers (Gray and Davisson, 2003):

$$\widetilde{\widetilde{H}}(\mathbf{x},\mathbf{x}') = \sum_{\mathbf{p}_r} \widetilde{\widetilde{H}}(\mathbf{x},\mathbf{x}',\mathbf{p}_r) \approx H(\mathbf{x},\mathbf{x}'). \tag{12}$$

For most practical applications where the number of shots is big, the randomly phase-encoded Hessian with one realization seems to be sufficient (Tang, 2009).

Regularizations

Regularization helps to stabilize the inversion; it can shape the null space and remove unwanted features in the inverted result by introducing user-defined model-covariance operators. In this paper, we choose to use the following regularization term:

$$\mathcal{R}(\mathbf{m}) = \frac{1}{2}||\mathbf{D}^*\mathbf{D}\mathbf{m}||^2, \tag{13}$$

where operator $\mathbf{D}$ contains wavekill filters (Claerbout, 2008), which annihilate local planar-events with given dips. The operator imposes continuity of reflectors along its dipping direction. This idea has also been explored by Clapp (2005) and Ayeni et al. (2009), who use similar filters (Clapp, 2003; Hale, 2007) to regularize the data-domain least-squares migration.

Instead of solving the inversion problem as a regularization problem, we solve it as a preconditioning problem by making change of variables as follows:

$$\mathbf{m} = \mathbf{S}\mathbf{n}, \tag{14}$$

where $\mathbf{n}$ is the vector of preconditioned variables and $\mathbf{S}$ is the preconditioning operator, which is defined to be an approximate inverse of the regularization operator $\mathbf{D}^*\mathbf{D}$. To find the inverse of $\mathbf{D}^*\mathbf{D}$, we factorize it into minimum-phase filters $\mathbf{A}$ such that $\mathbf{D}^*\mathbf{D} \approx \mathbf{A}^*\mathbf{A}$. We use the Wilson-Burg factorization (Claerbout, 1992; Fomel et al., 2003) and apply it on the helix (Claerbout, 1998, 2008). Since minimum-phase filters have stable inverses, we can define the preconditioning operator as follows:

$$\mathbf{S} = \mathbf{A}^{-1}\left(\mathbf{A}^*\right)^{-1}. \tag{15}$$

Unlike $\mathbf{D}^*\mathbf{D}$, operator $\mathbf{S}$ contains dip filters, which smooth along given dip directions. Substituting equations 13, 14 and 15 into 1 yields

$$J_p(\mathbf{n}) = \frac{1}{2}||\mathbf{H}\mathbf{S}\mathbf{n} - \mathbf{m}_{\text{mig}}||^2 + \epsilon||\mathbf{n}||^2. \tag{16}$$

Objective function 16 is often solved by setting $\epsilon = 0$ and iterating until an acceptable result is obtained (Claerbout, 2008). Solving it in this way implicitly assumes that we are starting with a model that has all the user-defined covariance, and that the more iterations we run, the more we honor the data. Once a solution vector $\mathbf{n}_{\text{sol}}$ has been found, the final model is obtained by computing $\mathbf{m}_{\text{sol}} = \mathbf{S}\mathbf{n}_{\text{sol}}$.

3-D FIELD-DATA EXAMPLES

We apply the target-oriented inversion method to a data set acquired from the Gulf of Mexico (GOM). The data set was acquired using a narrow-azimuth towed-streamer (NATS) acquisition system, and further rotated using azimuth moveout (AMO) (Biondi et al., 1998) into zero azimuth. The minimum and maximum inline offsets are 0.3 km and 8.2 km, respectively. The frequency content of the data set ranges between 5 Hz and 35 Hz. The velocity model used for migration and Hessian computation is shown in Figure 1, which is obtained using target-oriented wavefield tomography (Tang and Biondi, 2011).

We compute the migrated image using the 3-D conincal-wave migration operator, where we synthesize 101 conical waves for each crossline and migrate 12625 conical waves in total. The minimum and maximum inline take-off angles at the surface for the conical waves are $-30°$ and $30°$, respectively. The maximum frequency used for migration is 20 Hz. The image obtained for the target area is shown in Figure 2. Note that the amplitudes of the sediment reflectors are biased; also notice the illumination shadows below the salt due to the non-unitary characteristic of the Born modeling operator.

The 3-D Hessian matrix

We compute the phase-encoded Hessian using equations 6, 10 and 11. Since the number of shots is big, we compute only one random realization of the phase-encoded Hessian. The target region contains 784740 points, with 123 samples inline, 58 crossline and 110 in depth. The number of elements computed per row for the Hessian is 5155 (11 in x, 15 in y and 31 in z). Therefore, the widths of the local filter for each image point are 0.25 km, 0.35 km and 0.27 km in x, y and z directions, respectively. The top panels in Figures 3 and 4 present the diagonal components of the Hessian matrix at two different slices. Note that the values of the diagonal of the Hessian are far from uniform, and the left-side values are much higher than those elsewhere in the target region. This is because the salt body, which has relatively high velocities, prevents most of the energy from penetrating itself. The unevenness of the diagonal components also suggests that the Hessian matrix is highly nonstationary (each row is substantially different than the others). This is further illustrated by the bottom panels in Figures 3 and 4, which show the off-diagonal components of the Hessian matrix at two different image points. For an image point that is well illuminated

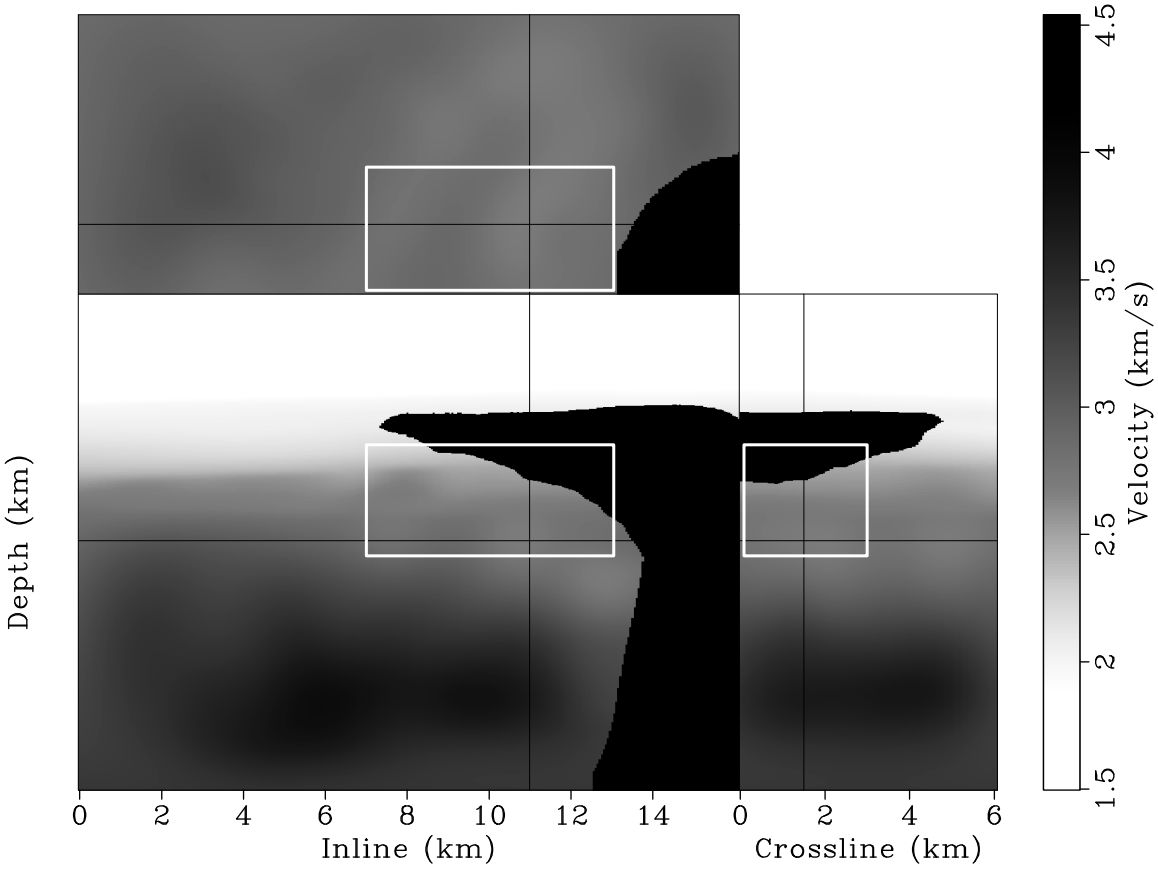

Figure 1: Target area selected (outlined by a box) for wavefield least-squares migration. [**CR**]

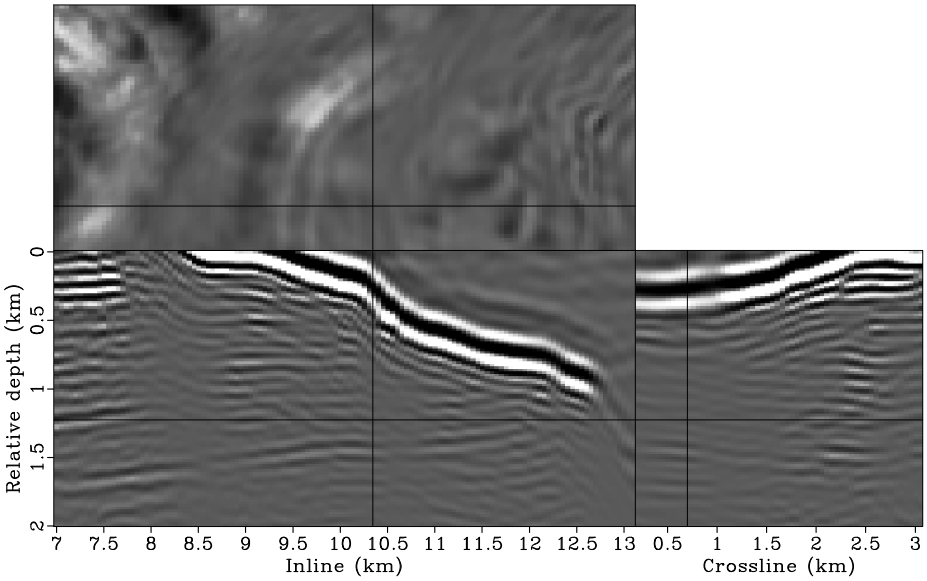

Figure 2: Migrated image for the selected target region. Note the illumination shadows below the salt. [**CR**]

(bottom panels in Figure 3), the off-diagonals have relatively wide spectrum coverage and are more focused around the diagonal. On the other hand, for an image point that is poorly illuminated (bottom panels in Figure 4), the off-diagonals have relatively narrow spectrum coverage and are more spread in the space domain.

To further appreciate the nonstationarities of the 3-D Hessian matrix, we apply the Hessian to a reflectivity model containing a collection of point scatterers (Figure 5). The result can also be considered as the filter response of the Hessian (where each row can be seen as a filter) to point scatterers. Note how the shape and strength of the filters change across the space. Also note that the filter is more elongated in the crossline direction than in the inline direction. This is a result of the single-azimuth acquisition geometry. Figure 6 shows the Hessian filter response for four horizontal reflectors. Note the imprint of shadow zones on the reflectors. The characteristics of the shadow zones very closely match those in the migrated image (Figure 2), indicating that the computed Hessian matrix, albeit with some approximations, accurately captures the effects of uneven subsurface illumination due to limited acquisition geometry, band-limited wave phenomena and complex overburden. In the subsequent section, I demonstrate how the effects of uneven illumination can be optimally removed by inverting the Hessian matrix through regularized linear inversion.

Inversion result

Since the goal is to invert sediment reflectivities, we incorporate a mask operator (Figure 7) into the inversion to prevent updating the reflectivities of the salt boundary. We first run the inversion without applying any regularizations; the inverted image after 100 iterations is shown in Figure 9. Compared to migration (Figure 8), inversion significantly improves the spatial resolution of the image; the amplitudes are more balanced, and the illumination shadows are filled in. However, the inverted image is more noisy, and the continuity of the reflectors seems to be degraded. The increased noise level reveals the ill-posedness of the inversion problem due to the narrow bandwidth of the Hessian filter (bottom panels of Figures 3 and 4). Another reason might be that the approximations used to compute the Green's function (acoustic one-way wave equation) and the migration do not fully match the way seismic waves propagate through the earth. The inconsistency of the operator and the data may further increase the ill-posedness of the inversion problem. Therefore, regularization becomes necessary.

In order to regularize the inversion with a reasonably accurate model covariance, we interpret the migrated image and manually pick several key reflectors (Figure 10). We estimate dip fields based on the interpreted reflectors using the structure tensor method (van Vliet and Verbeek, 1995; Hale, 2007). The estimated dips have been smoothed with a triangle filter and are shown in Figure 11. The dip field is then used to build a bank of dip filters for preconditioning. Figures 12, 13 and 14 show impulse responses of the dip filters as smoothing strength increases. Note that the stronger the smoothing effect, the longer the filter response. These dip filters also vary

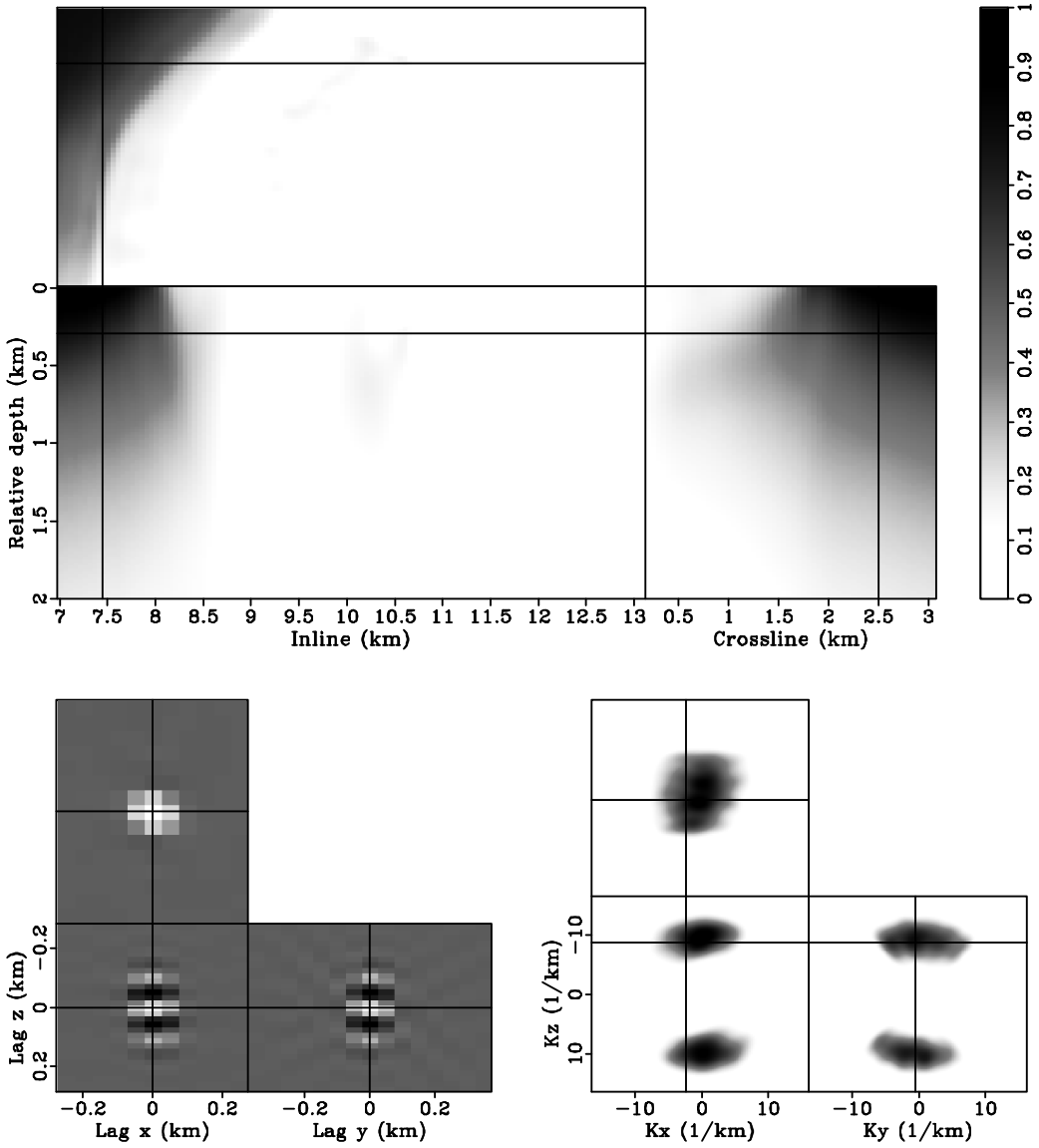

Figure 3: The Hessian matrix for the target region. The top panel shows the diagonal components of the matrix; the bottom left panel shows the off-diagonals of the matrix taken from the image point at inline 7.45 km, crossline 2.50 km and relative depth 0.30 km (the intersection of the crosshairs in the top panel); the bottom right panel shows the amplitude spectrum of the off-diagonal components. [**CR**]

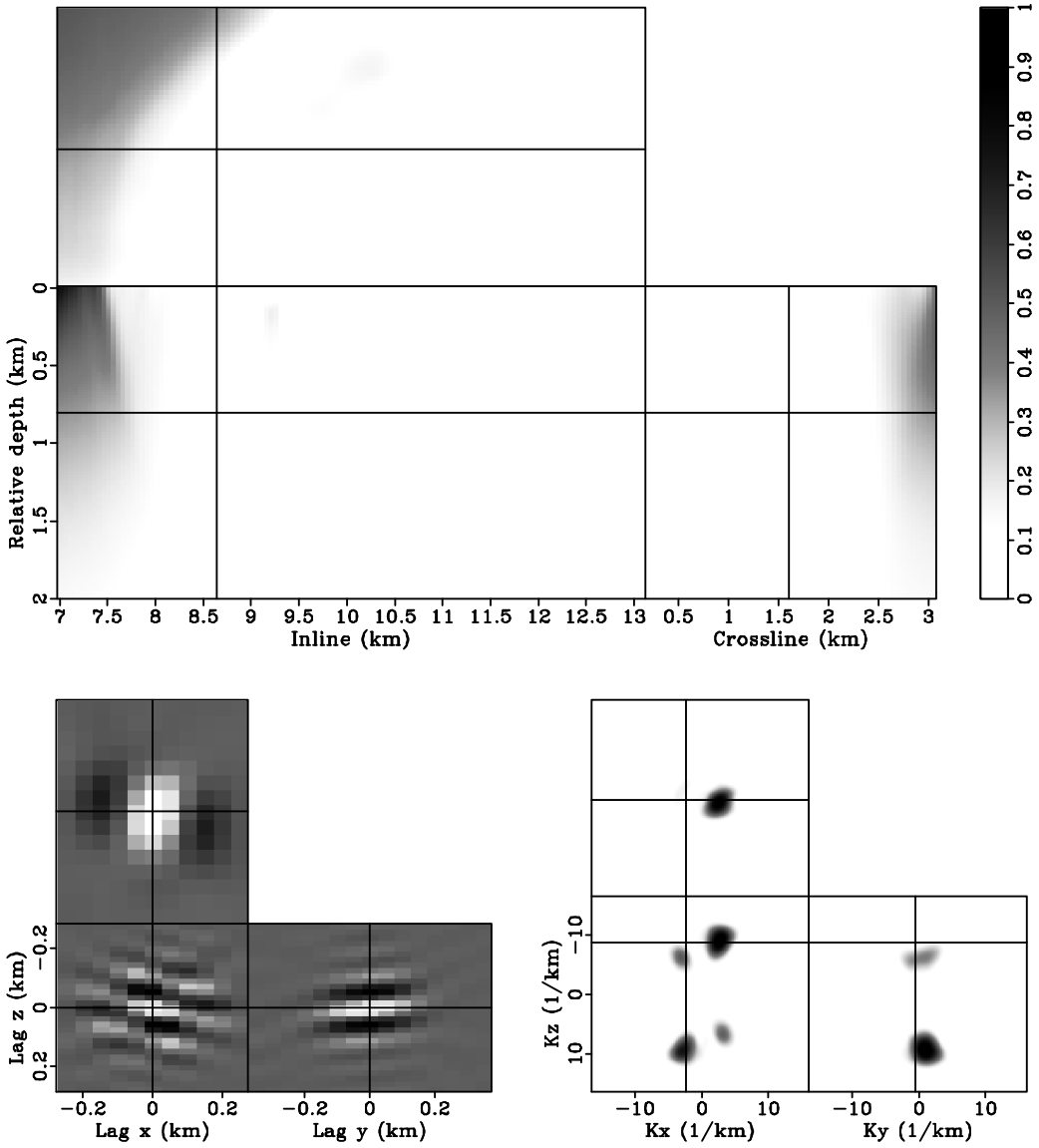

Figure 4: The Hessian matrix for the target region. The top panel shows the diagonal components of the matrix; the bottom left panel shows the off-diagonals of the matrix taken from the image point at inline 8.65 km, crossline 1.60 km and relative depth 0.80 km (the intersection of the crosshairs in the top panel); the bottom right panel shows the amplitude spectrum of the off-diagonal components. [**CR**]

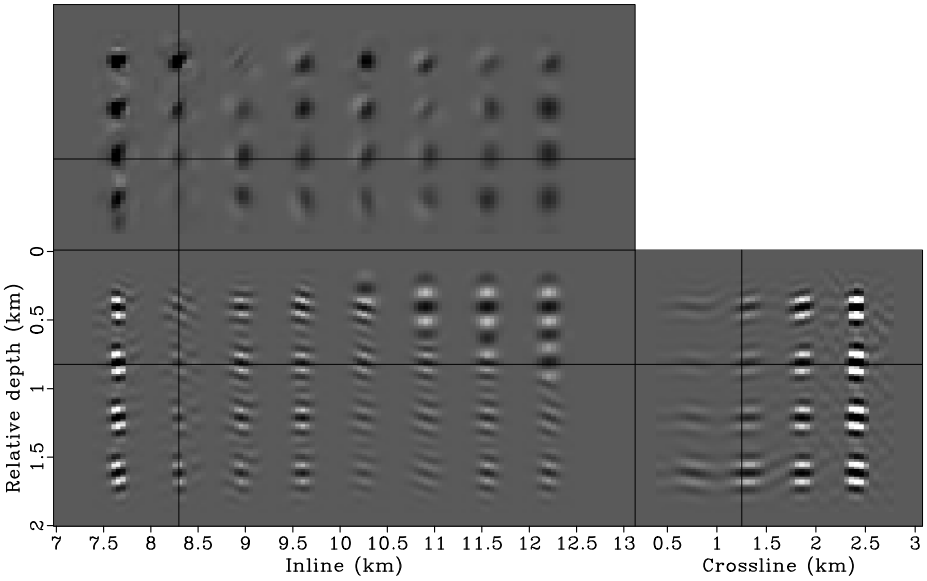

(a)

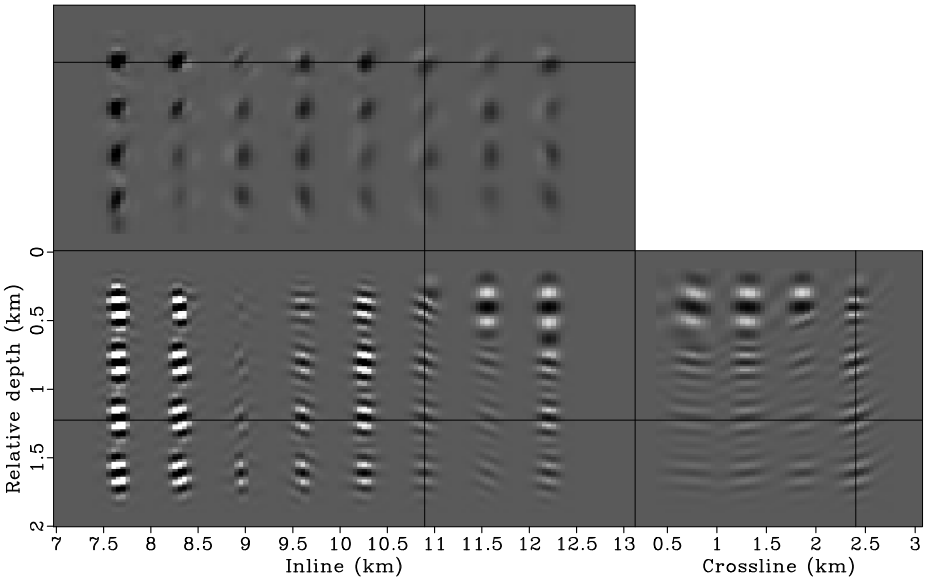

(b)

Figure 5: Hessian filter response for point scatterers. Panels (a) and (b) show different slices of the same 3-D cube. Note the nonstationarity of the filters. [**CR**]

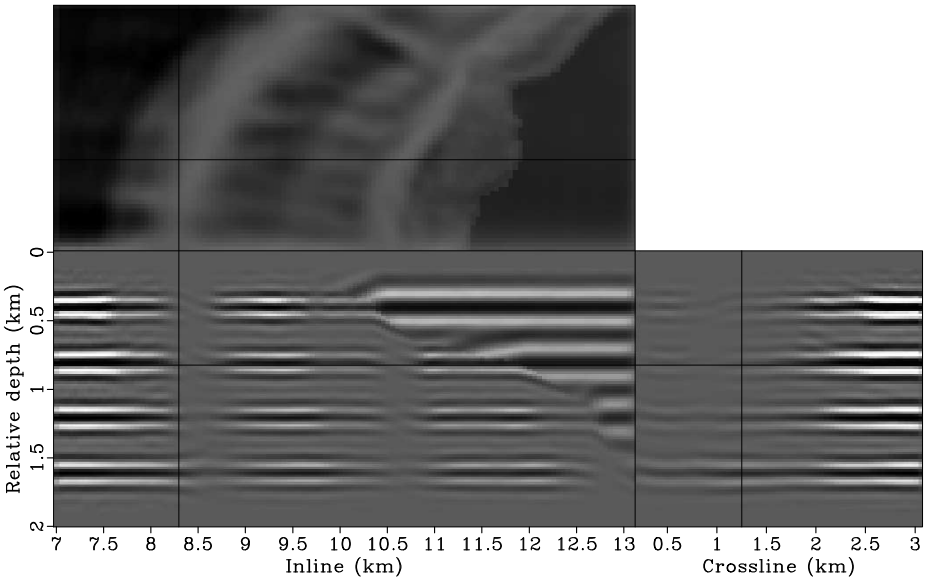

(a)

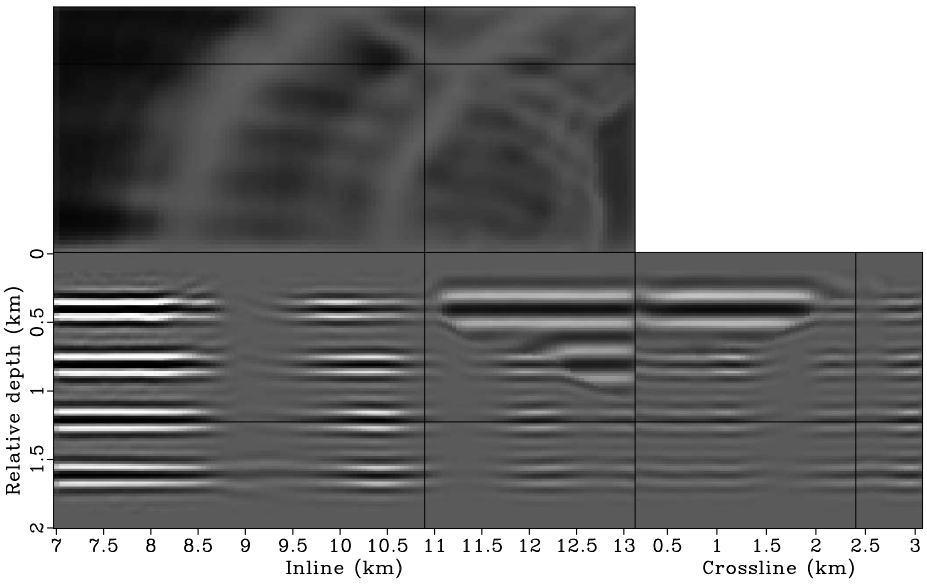

(b)

Figure 6: Hessian filter response for horizontal reflectors. Panels (a) and (b) show different slices of the same 3-D cube. Note the imprint of shadow zones on the reflectors. [**CR**]

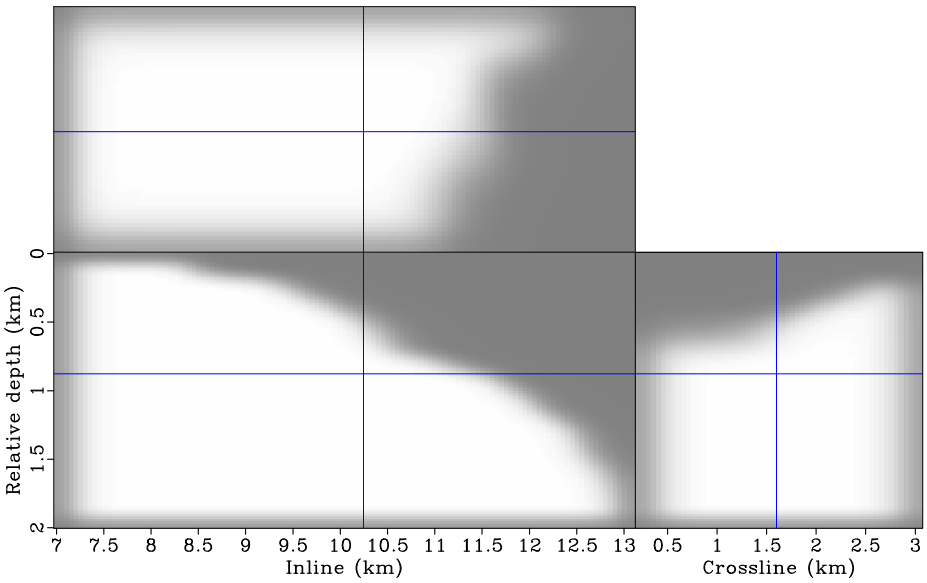

Figure 7: A mask operator used during inversion. [**CR**]

spatially, and each dip filter smooths along a direction conformal to the corresponding dip values.

Figure 15 presents the inverted image after 100 iterations when preconditioned by the dip filter with weak smoothing (Figure 12). The result is significantly improved over the one obtained without any regularizations (Figure 9). The reflectors are much more coherent and they extend further into the shadow zone, filling in the illumination gap almost completely. The regularized image is much easier to interpret geologically.

To see the effects of regularization (or preconditioning), we increase the smoothing strength of the dip filters. Figure 16 shows the inversion result after 100 iterations when we use dip filters with moderate smoothing (Figure 12) for preconditioning. The result further enhances the coherence and continuity of the reflectors and the inverted image looks even cleaner. However, the spatial resolution of the image seems somewhat degraded by the smoothing effect of the preconditioner (This becomes clear by comparing the depth slices of Figures 9, 15 and 16).

Figure 17 shows the inversion result when we further increase the smoothing strength of the dip filters (Figure 14). In this extreme case, inversion is dominated by preconditioning. The inverted image honors the user-supplied model-covariance, but not necessarily the data. (The data fitting plays little role in this case.)

Figures 18 and 19 compare the residuals at the last iteration and the convergence of objective functions for different methods. As expected, inversion without any regularization, which fits the data most closely, has the smallest residual, whereas inversion preconditioned with strong dip filters, which fits the data least closely, has the biggest residual.

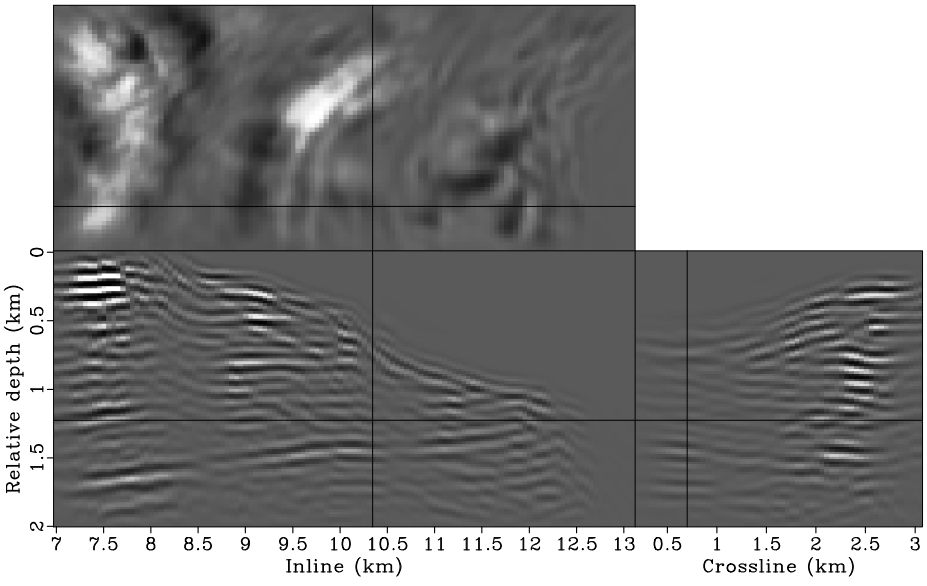

(a)

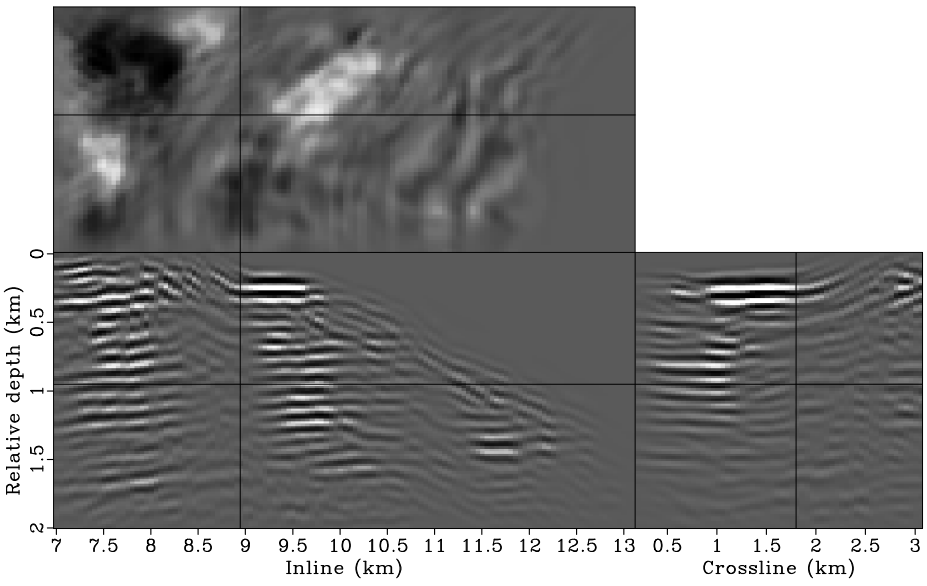

(b)

Figure 8: The migrated image of the 3-D GOM data set. Panels (a) and (b) show different slices of the same 3-D cube. The image has been masked using the mask operator shown in Figure 7 to focus on comparing sediment reflectivities. [**CR**]

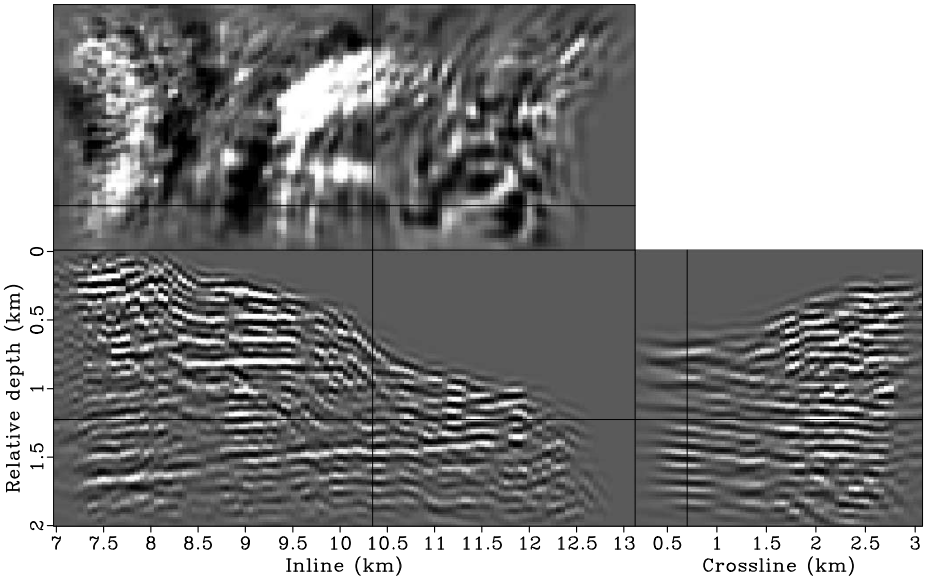

(a)

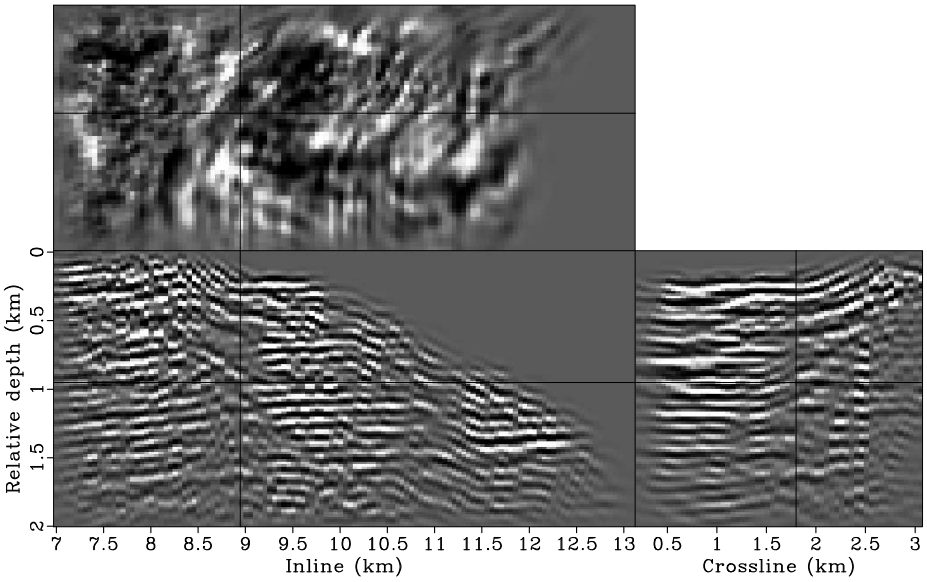

(b)

Figure 9: The inverted image without applying any regularization. Panels (a) and (b) show different slices of the same 3-D cube. [**CR**]

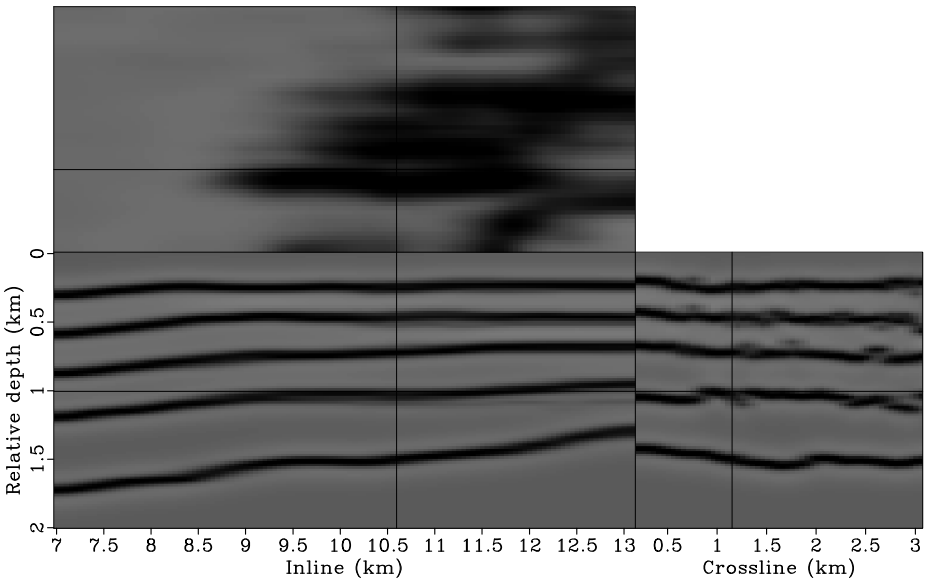

Figure 10: Interpreted horizons from the migrated image. The horizons are then used to build the dip field for dip filtering. [**CR**]

CONCLUSIONS

Solving wavefield least-squares migration in the image domain makes possible target-oriented application of this method, allowing reflectivity inversion at the reservoir level. The 3-D examples demonstrate that simultaneous phase-encoding in the conical-wave domain drastically reduces the computational cost of the 3-D Hessian matrix. The phase-encoded Hessian, albeit with some approximations, accurately quantifies the illumination effects on the migrated image. Since inverting the Hessian is very fast, different regularization parameters or schemes can be tried at very low cost. For the 3-D example shown in this chapter, it takes only about 6 minutes to run 100 iterations using 34 CPUs (17 nodes with 2 cores on each). This is a very important advantage over the conventional data-domain implementation, which requires full-domain modeling and migration at each iteration. The high efficiency of this method also makes interactive reflectivity imaging possible, where we can repeat the inversion with regularizations that incorporate different geological scenarios and obtain the results in almost real time. The 3-D reflectivity inversion results illustrate that inversion preconditioned with dip filters successfully recovers the reflectivity from the effects of uneven illumination, yielding more balanced amplitudes and higher spatial resolution in the inverted image.

ACKNOWLEDGEMENTS

We thank Gboyega Ayeni for insightful discussion about dip filtering. We acknowledge BP and ExxonMobil for providing the field data set. We also thank the Stanford

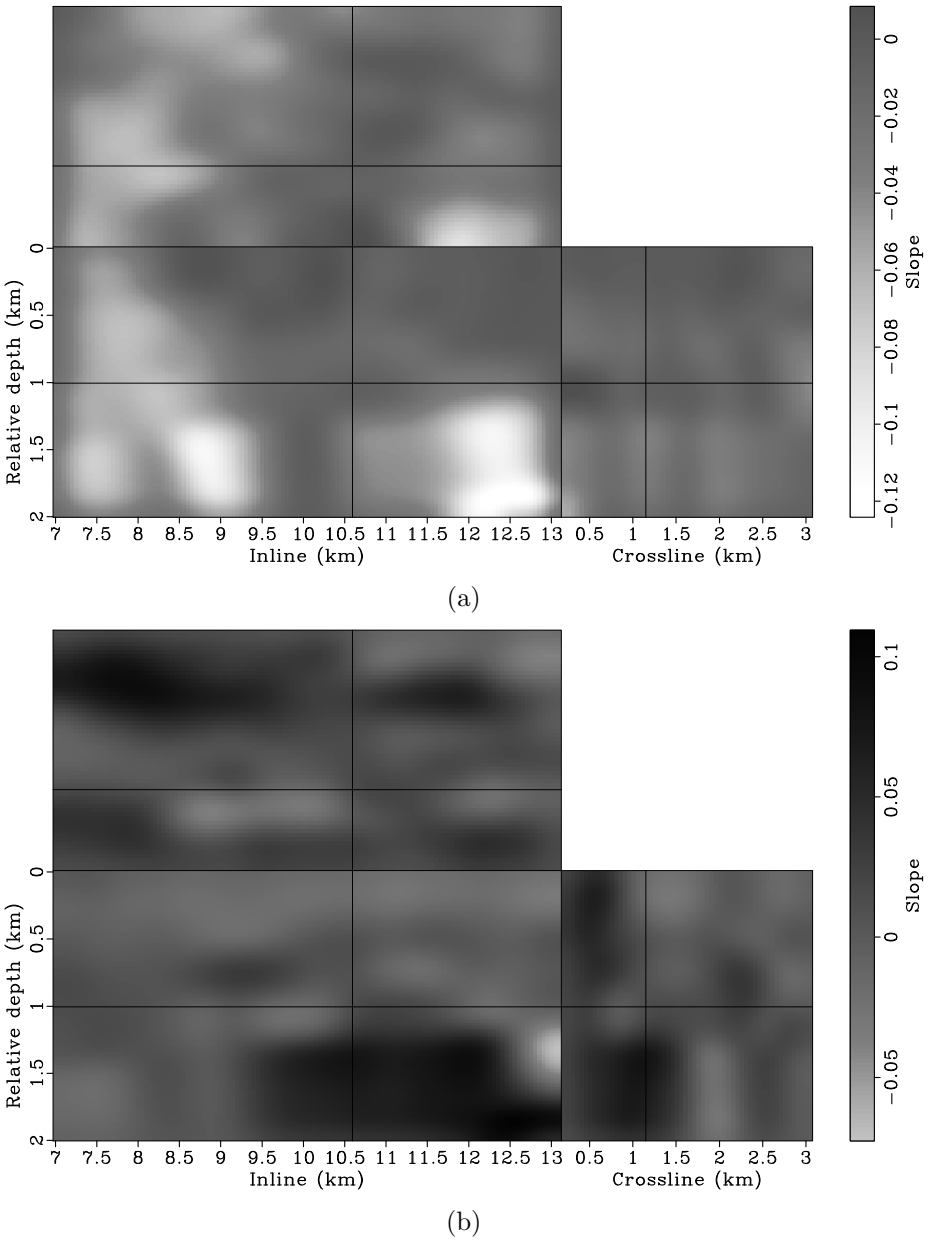

Figure 11: The estimated dip field from the interpreted reflectors. Panels (a) and (b) are the slopes in the inline and crossline directions, respectively. [**CR**]

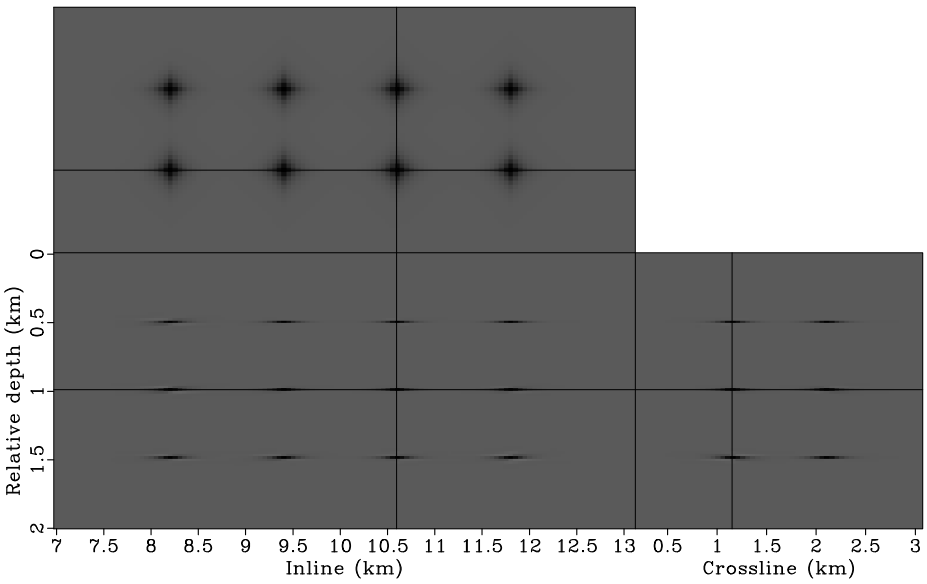

Figure 12: Impulse responses of the dip filters with weak smoothing. [**CR**]

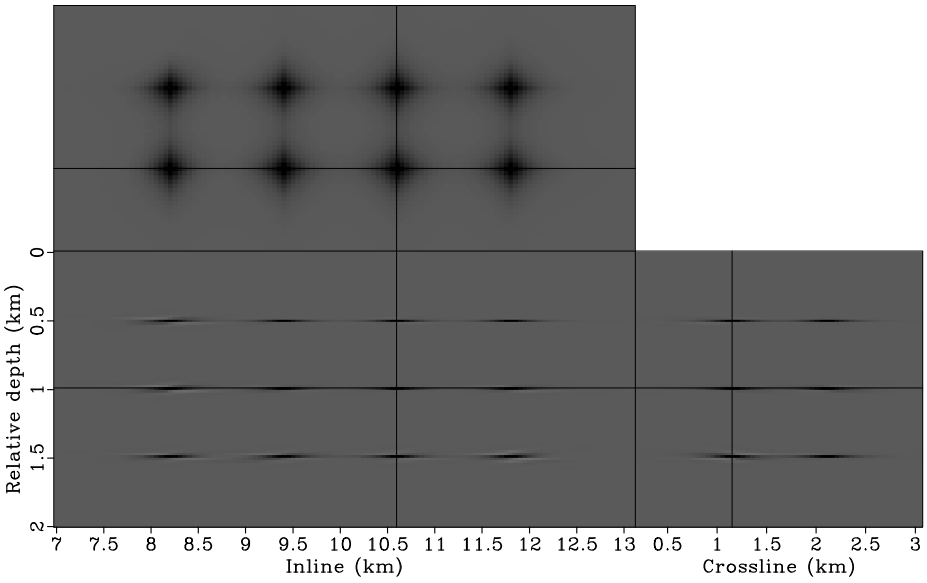

Figure 13: Impulse responses of the dip filters with moderate smoothing. [**CR**]

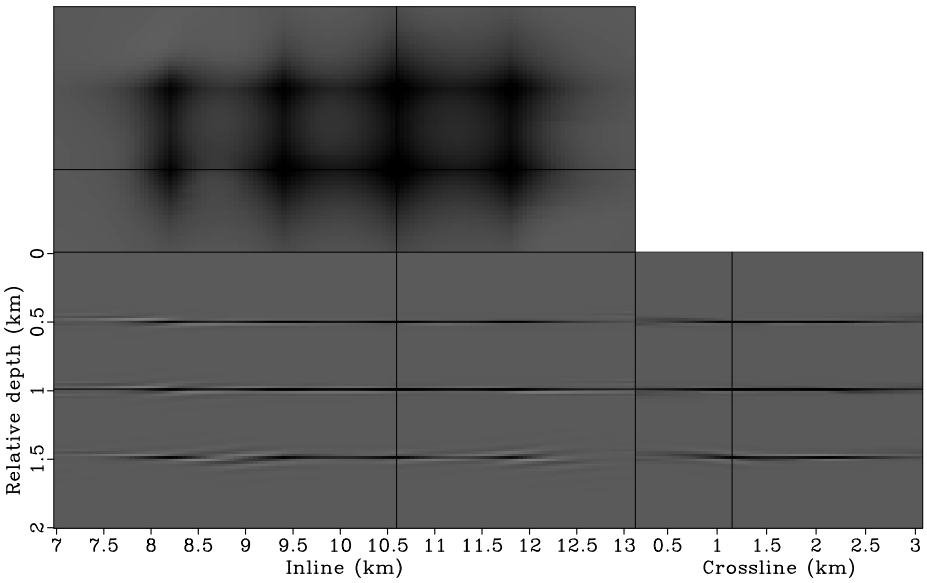

Figure 14: Impulse responses of the dip filters with strong smoothing. [**CR**]

Center for Computational Earth and Environmental Science for providing computing resources.

REFERENCES

Ayeni, G., Y. Tang, and B. Biondi, 2009, Joint preconditioned least-squares inversion of simultaneous source time-lapse seismic data sets: SEG Technical Program Expanded Abstracts, **28**, 3914–3918.

Biondi, B., S. Fomel, and N. Chemingui, 1998, Azimuth moveout for 3-d prestack imaging: Geophysics, **63**, 574–588.

Claerbout, J., 1998, Multidimensional recursive filters via a helix: Geophysics, **63**, 1532–1541.

Claerbout, J. F., 1985, Imaging the earth's interior: Blackwell Scientific Publication.

———, 1992, Earth soundings analysis: Processing versus inversion: Blackwell Scientific Publication.

———, 2008, Image Estimation By Example: Geophysical Sounding Image Construction: Multidimensional Autoregression: Stanford University.

Clapp, M. L., 2005, Imaging Under Salt: Illumination Compensation by Regularized Inversion: PhD thesis, Stanford University.

Clapp, R., 2003, Geologically Constrained Migration Velocity Analysis: PhD thesis, Stanford University.

Duquet, B., P. Lailly, and A. Ehinger, 2001, 3d plane wave migration of streamer data: SEG Technical Program Expanded Abstracts, **20**, 1033–1036.

Fomel, S., P. Sava, J. Rickett, and J. F. Claerbout, 2003, The wilsonburg method of spectral factorization with application to helical filtering: Geophysical Prospecting,

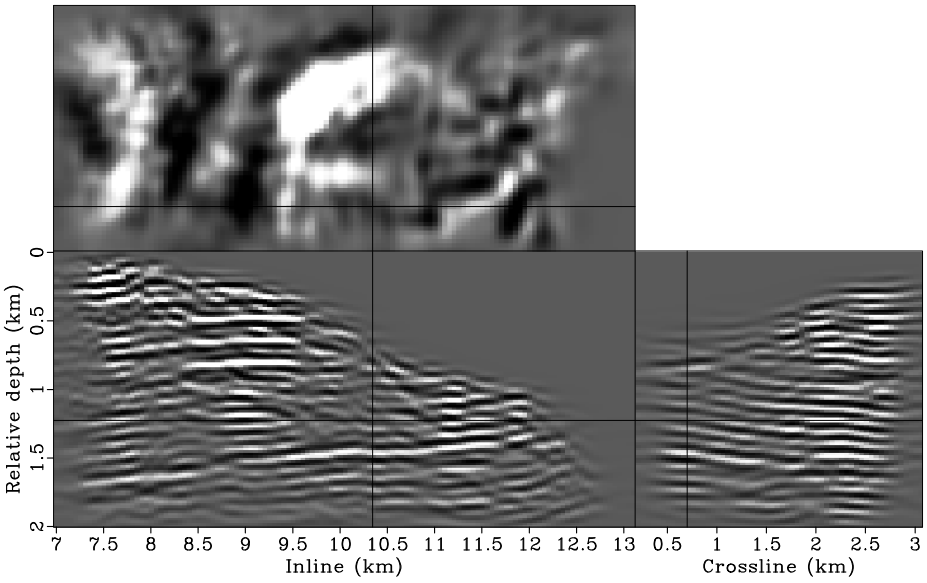

(a)

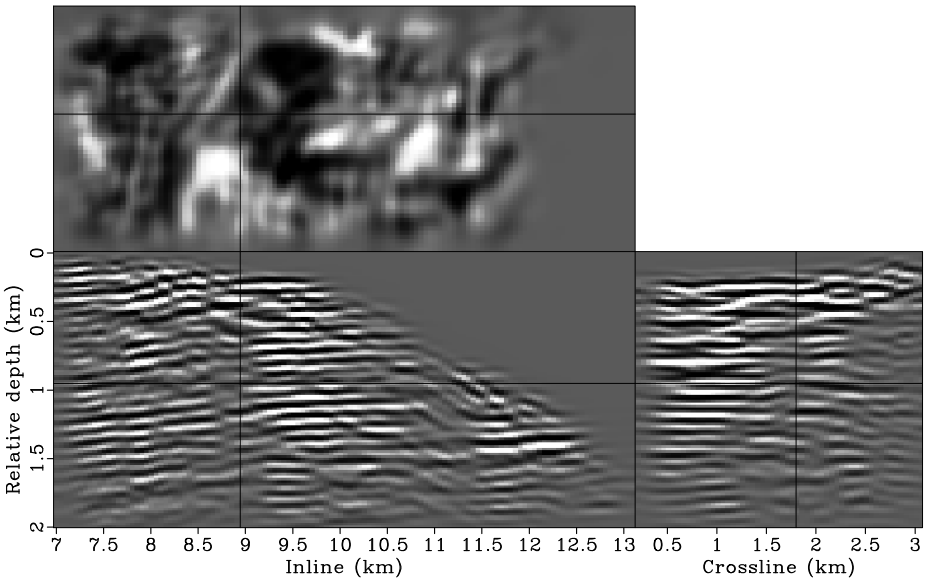

(b)

Figure 15: The inverted image when preconditioned using dip filters with weak smoothing (Figure 12). [**CR**]

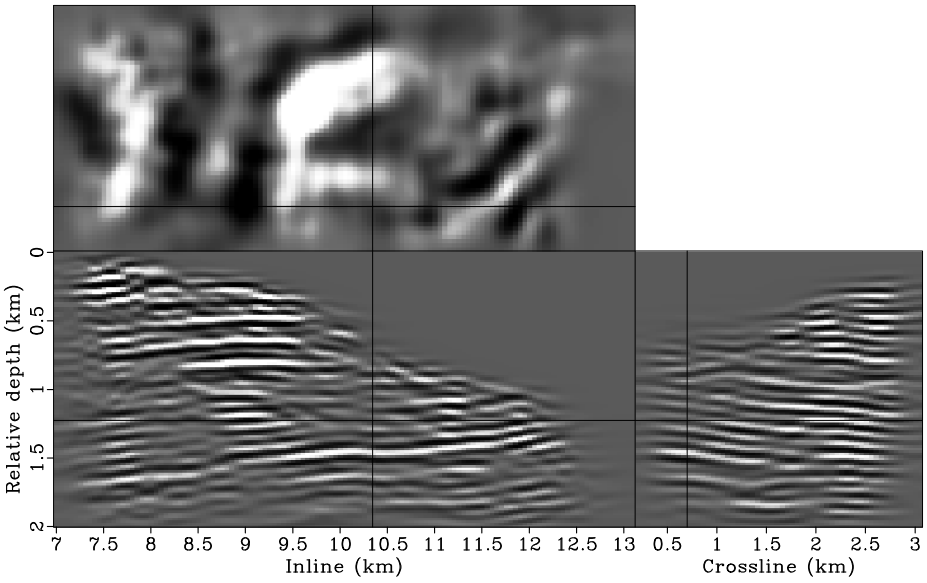

(a)

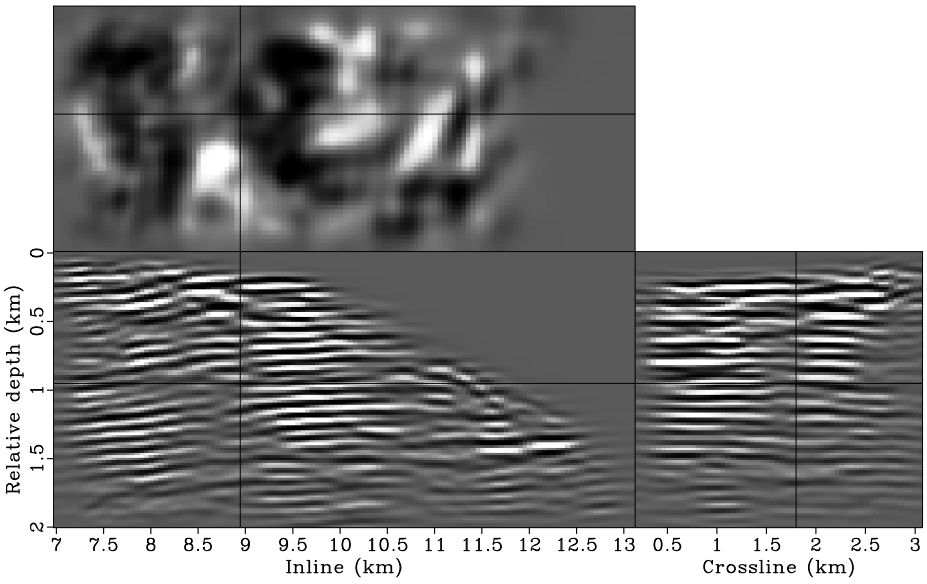

(b)

Figure 16: The inverted image when preconditioned using dip filters with moderate smoothing (Figure 13). [**CR**]

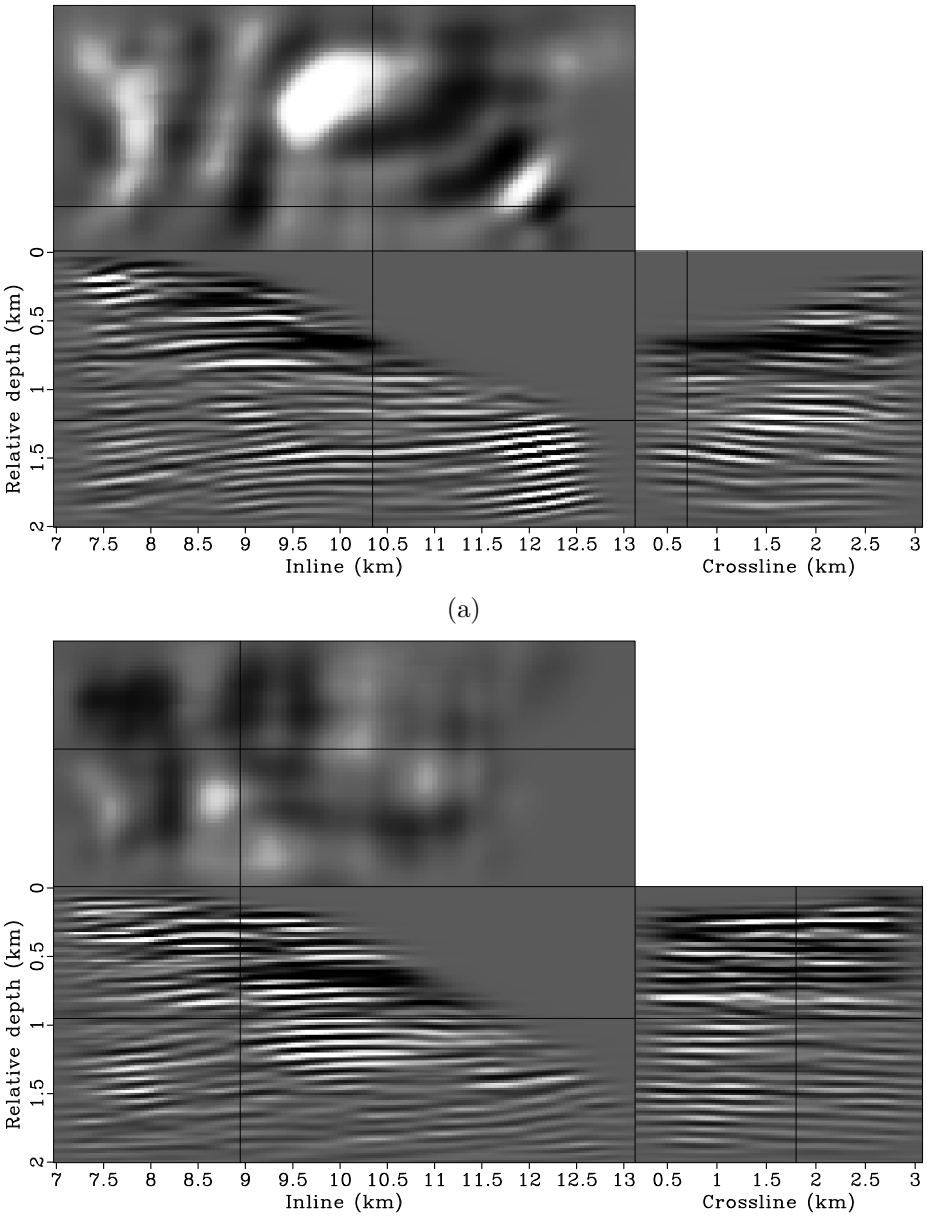

Figure 17: The inverted image when preconditioned using dip filters with strong smoothing (Figure 14). [**CR**]

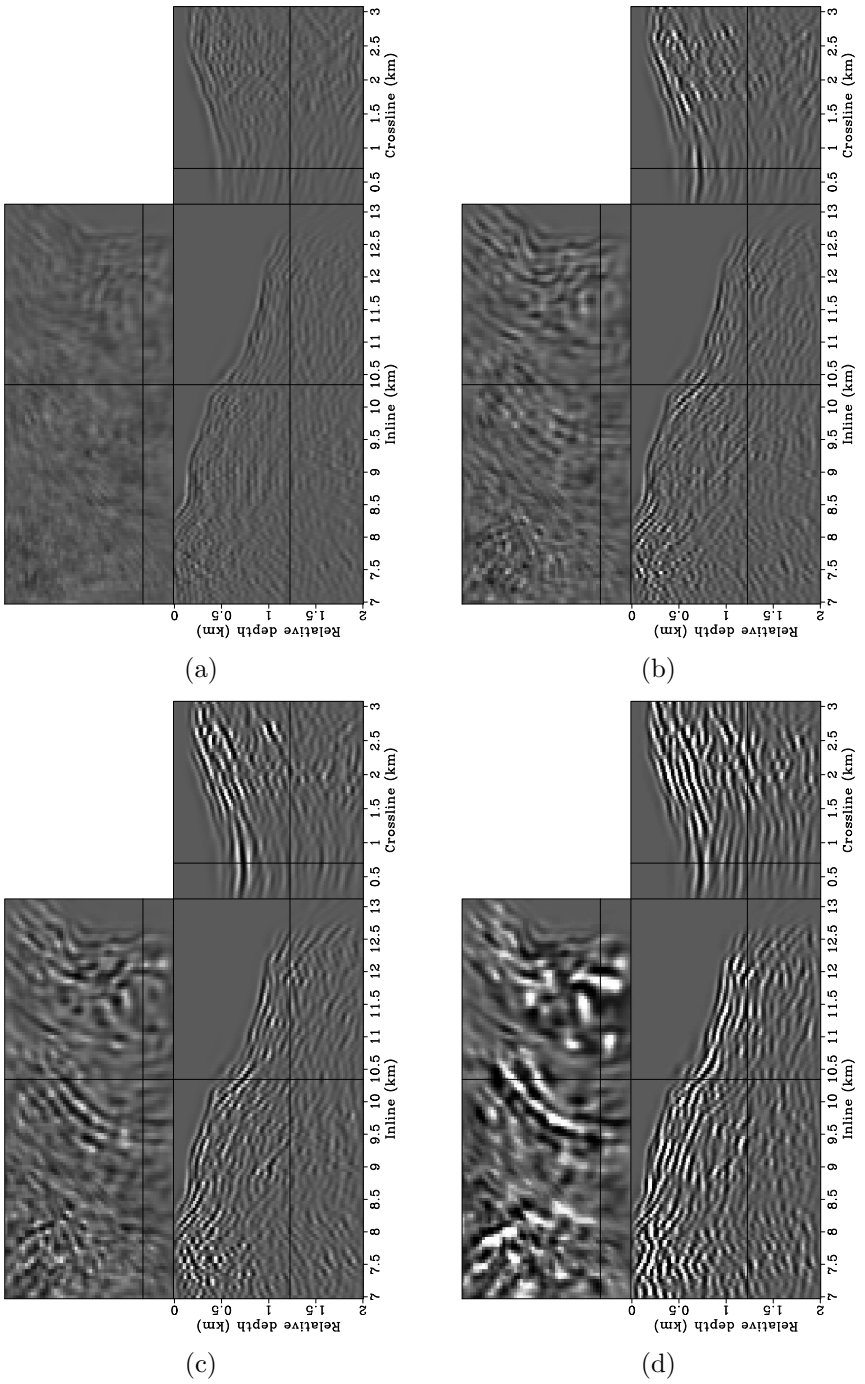

Figure 18: Residuals at the last iteration for different methods. Panel (a) is obtained using inversion without regularization. Panels (b), (c) and (d) are obtained using inversion preconditioned with weak, moderate and strong dip filtering, respectively. All panels are clipped to the same value. [**CR**]

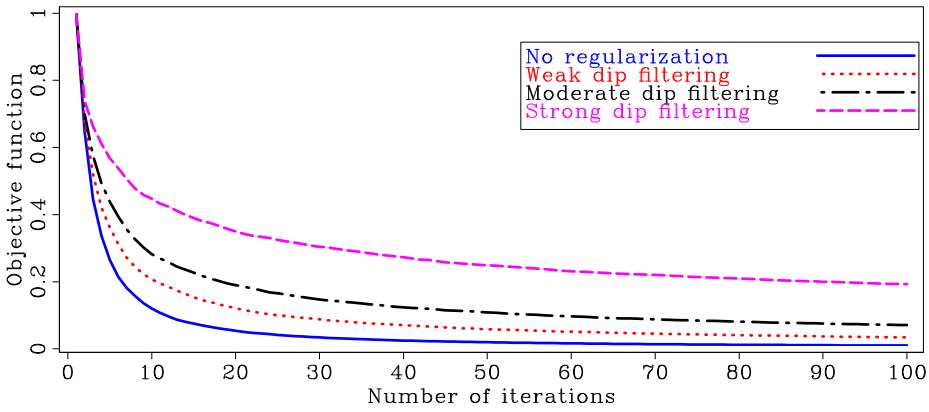

Figure 19: Evolution of objective functions for different inversion methods. [**CR**]

51, 409–420.

Gray, R. and L. D. Davisson, 2003, Introduction to Statistical Signal Processing: Cambridge University Press.

Hale, D., 2007, Local dip filtering with directional laplacians: CWP Project Review, **567**, 91–102.

Kühl, H. and M. D. Sacchi, 2003, Least-squares wave-equation migration for avp/ava inversion: Geophysics, **68**, 262–273.

Lailly, P., 1983, The seismic inverse problem as a sequence of before stack migration: Proc. Conf. on Inverse Scattering, Theory and Applications, Expanded Abstracts, Philadelphia, SIAM.

Lecomte, I., 2008, Resolution and illumination analyses in PSDM: A ray-based approach: The Leading Edge, **27**, no. 5, 650–663.

Liu, F., D. W. Hanson, N. D. Whitmore, R. S. Day, and R. H. Stolt, 2006, Toward a unified analysis for source plane-wave migration: Geophysics, **71**, no. 4, S129–S139.

Nemeth, T., C. Wu, and G. T. Schuster, 1999, Least-squares migration of incomplete reflection data: Geophysics, **64**, 208–221.

Stolt, R. H. and A. Benson, 1986, Seismic Migration: Theory and Practice: Geophysical Press.

Tang, Y., 2009, Target-oriented wave-equation least-squares migration/inversion with phase-encoded Hessian: Geophysics, **74**, WCA95–WCA107.

Tang, Y. and B. Biondi, 2011, Subsalt velocity analysis by target-oriented wavefield tomography: A 3-D field-data example: **SEP-143**, xxx–xxx.

Tang, Y. and S. Lee, 2010, Preconditioning full waveform inversion with phase-encoded hessian: SEG Technical Program Expanded Abstracts, **29**, 1034–1038.

Valenciano, A., 2008, Imaging by Wave-equation Inversion: PhD thesis, Stanford University.

van Vliet, L. J. and P. W. Verbeek, 1995, Estimators for orientation and anisotropy in digitized images: ASCI95, Proc. First Annual Conference of the Advanced School for Computing and Imaging (Heijen, NL, May 16-18), ASCI, 442–450.

Whitmore, N. D., 1995, An Imaging Hierarchy for Common Angle Plane Wave Seis-

mogram: PhD thesis, University of Tulsa.
Zhang, Y., J. Sun, C. Notfors, S. H. Gray, L. Chernis, and J. Young, 2005, Delayed-shot 3d depth migration: Geophysics, **70**, E21–E28.

APPENDIX A

3-D CONICAL-WAVE DOMAIN HESSIAN

In general, a 3-D surface seismic data set can be represented by a 5-D object $d(\mathbf{x}_r, \mathbf{x}_s, \omega)$, with $\mathbf{x}_r = (x_r, y_r, z_r = 0)$ and $\mathbf{x}_s = (x_s, y_s, z_s = 0)$ being the receiver and source position, respectively, and ω being the angular frequency. Under the Born approximation (Stolt and Benson, 1986), the data can be modeled by a linear operator as follows:

$$d(\mathbf{x}_r, \mathbf{x}_s, \omega) = \sum_{\mathbf{x}} \omega^2 f_s(\omega) G(\mathbf{x}, \mathbf{x}_s, \omega) G(\mathbf{x}, \mathbf{x}_r, \omega) m(\mathbf{x}), \tag{A-1}$$

where $f_s(\omega)$ is the source function; $G(\mathbf{x}, \mathbf{x}_s, \omega)$ and $G(\mathbf{x}, \mathbf{x}_r, \omega)$ are the Green's functions connecting the source and receiver position to the image point $\mathbf{x} = (x, y, z)$, respectively. We can transform data into the conical-wave domain by slant-stacking along the inline source axis x_s as follows:

$$d(\mathbf{x}_r, p_{s_x}, y_s, \omega) = \sum_{x_s} W(\mathbf{x}_r, x_s, y_s) d(\mathbf{x}_r, x_s, y_s, \omega) \mathrm{e}^{i\omega p_{s_x} x_s}, \tag{A-2}$$

where $W(\mathbf{x}_r, x_s, y_s)$ is the acquisition mask operator, which contains ones where we record data, and zeros where we do not; p_{s_x} is the surface ray parameter in the inline direction. The inverse transform is

$$W(\mathbf{x}_r, x_s, y_s) d(\mathbf{x}_r, x_s, y_s, \omega) = |\omega| \sum_{p_{s_x}} d(\mathbf{x}_r, p_{s_x}, y_s, \omega) \mathrm{e}^{-i\omega p_{s_x} x_s}, \tag{A-3}$$

where $|\omega|$ on the right hand side of the equation is also known as the "rho" filter (Claerbout, 1985).

To find a reflectivity model $\mathbf{m}$ that best fits the observed data for a given background velocity, we can minimize a data-misfit function that measures the differences between the observed data and the synthesized data in a least-squares sense. In the point-source case, the data-misfit function is

$$F(\mathbf{m}) = \frac{1}{2} \sum_{\omega} \sum_{\mathbf{x}_s} \sum_{\mathbf{x}_r} |W(\mathbf{x}_r, \mathbf{x}_s)[d(\mathbf{x}_r, \mathbf{x}_s, \omega) - d_{\mathrm{obs}}(\mathbf{x}_r, \mathbf{x}_s, \omega)]|^2, \tag{A-4}$$

where d_{obs} is the observed data. Substituting equation A-3 into A-4 yields

$$\begin{aligned} F(\mathbf{m}) \;=\; & \frac{1}{2} \sum_{\omega} \sum_{y_s} \sum_{\mathbf{x}_r} \sum_{p_{s_x}} \sum_{p'_{s_x}} |\omega|^2 \\ & \times [d(\mathbf{x}_r, p_{s_x}, y_s, \omega) - d_{\mathrm{obs}}(\mathbf{x}_r, p_{s_x}, y_s, \omega)]^* \\ & \times [d(\mathbf{x}_r, p'_{s_x}, y_s, \omega) - d_{\mathrm{obs}}(\mathbf{x}_r, p'_{s_x}, y_s, \omega)] \sum_{x_s} e^{-i\omega(p'_{s_x} - p_{s_x}) x_s}. \end{aligned} \tag{A-5}$$

If the inline source axis x_s is reasonably well sampled, we have $\sum_{x_s} e^{-i\omega(p'_{s_x}-p_{s_x})x_s} \approx \frac{1}{|\omega|}\delta(p'_{s_x}-p_{s_x})$, where $\delta(\cdot)$ is the Dirac delta function. Therefore, an objective function equivalent to equation A-4 in the 3-D conical-wave domain takes the following form:

$$F(\mathbf{m}) \approx \frac{1}{2}\sum_{\omega}|\omega|\sum_{y_s}\sum_{p_{s_x}}\sum_{\mathbf{x}_r}|d(\mathbf{x}_r,p_{s_x},y_s,\omega)-d_{\text{obs}}(\mathbf{x}_r,p_{s_x},y_s,\omega)|^2. \tag{A-6}$$

The Hessian operator in the 3-D conical-wave domain can be obtained by taking the second-order derivatives of $F(\mathbf{m})$ (equation A-6) with respect to the model parameters:

$$H(\mathbf{x},\mathbf{x}') = \sum_{\omega}|\omega|^5\sum_{y_s}\sum_{p_{s_x}}\sum_{\mathbf{x}_r}\left(\frac{\partial d(\mathbf{x}_r,p_{s_x},y_s,\omega)}{\partial m(\mathbf{x})}\right)\left(\frac{\partial d(\mathbf{x}_r,p_{s_x},y_s,\omega)}{\partial m(\mathbf{x}')}\right)^*. \tag{A-7}$$

When $\mathbf{x}=\mathbf{x}'$, we obtain the diagonal components of the Hessian, which are also known as the subsurface illumination; otherwise, we obtain the off-diagonal components of the Hessian, which are also known as the resolution function for a given acquisition setup.

With equations A-1 and A-2, we obtain the expression of the derivative of d with respect to m as follows:

$$\begin{aligned}\frac{\partial d(\mathbf{x}_r,p_{s_x},y_s,\omega)}{\partial m(\mathbf{x})} &= \sum_{x_s}\omega^2 W(\mathbf{x}_r,x_s,y_s)f_s(\omega)G(\mathbf{x},x_s,y_s,\omega)\\ &\quad\times G(\mathbf{x},\mathbf{x}_r,\omega)\mathrm{e}^{i\omega p_{s_x}x_s}.\end{aligned} \tag{A-8}$$

Substituting equation A-8 into equation A-7 yields the expression for each component of the Hessian matrix in the 3-D conical-wave domain:

$$\begin{aligned}H(\mathbf{x},\mathbf{x}') &= \sum_{\omega}|\omega|^5\sum_{y_s}\sum_{p_{s_x}}\sum_{\mathbf{x}_r}G(\mathbf{x},\mathbf{x}_r,\omega)G^*(\mathbf{x}',\mathbf{x}_r,\omega)\\ &\quad\sum_{x_s}W(\mathbf{x}_r,x_s,y_s)f_s(\omega)G(\mathbf{x},x_s,y_s,\omega)\mathrm{e}^{i\omega p_{s_x}x_s}\\ &\quad\sum_{x'_s}W(\mathbf{x}_r,x'_s,y_s)f^*_s(\omega)G^*(\mathbf{x}',x'_s,y_s,\omega)\mathrm{e}^{-i\omega p_{s_x}x'_s}.\end{aligned} \tag{A-9}$$